

Seeding-free inlet flow distortion measurement by filtered Rayleigh scattering: diagnostic approach and verification

Ulrich Doll*, Ralf Kapulla†

Experimental Thermal Hydraulics Group, Paul Scherrer Institute, Forschungstrasse 111, Villigen PSI, 5232, Switzerland

Jonas J. Steinbock‡, Michael Dues§

ILA R&D GmbH, Rudolf-Schulten-Straße 3, Jülich, 52428, Germany

Matteo Migliorini¶, Pavlos K. Zachos||

Centre for Propulsion and Thermal Power Engineering, Cranfield University, MK43 0AL, Cranfield, United Kingdom

The expected close coupling between engine and fuselage of future aero-engine architectures will lead to highly distorted inflows at the engine face, presenting a major design risk for efficient and reliable engine operation. In particular, the increase in flow unsteadiness is perceived as a significant challenge. In this context, the Cranfield Complex Intake Test Facility (CCITF) is currently being installed at Cranfield University to reproduce the anticipated level of total pressure and swirl distortion arising from novel, closely coupled airframe-engine configurations. To address the expected demand for much more comprehensive flow field data, it is intended to establish the filtered Rayleigh scattering (FRS) technique for non-intrusive testing of aero-engine intake flows. Unlike the previously used particle image velocimetry (PIV) or Doppler global velocimetry (DGV), which are limited to the measurement of a single flow quantity, FRS can be used for the combined planar measurement of velocity and scalar fields without the need to add a flow tracer. In this study, an FRS concept with the ability to simultaneously measure high-accuracy time-averaged and time-resolved three-component velocity, static pressure and temperature fields is verified on a simplified mock-up of the CCITF facility. Time-averaged results show excellent agreement with benchmark laser Doppler anemometry (LDA) velocities, static pressure probe measurements and analytical temperature calculations. Moreover, it is shown that the developed concept can be used to determine multiple flow variables from a single-frequency measurement, opening the path towards time-resolved multi-parameter measurements by FRS.

I. Introduction

To comply with aviation's emission targets set out in the strategic agendas by the European Commission, NASA and ACARE [1–3], future aircraft designs will require a close integration of the propulsion system into the airframe to benefit from promising fuel-saving concepts such as boundary layer ingestion (BLI) or distributed propulsion [4–6]. Major design challenges arise from the interaction of fuselage boundary layer and convoluted intake geometry, leading to a high level of both steady and unsteady inlet flow distortion (total pressure and swirl) at the engine face [7–11]. In view of the expected unsteadiness and angularity of the resulting total pressure and velocity fields, the established measurement strategies relying on intrusive pressure rakes are too limited in their spatial and temporal resolution to capture the relevant flow effects, as outlined in the SAE ARP1420 aerospace standard [12]. As a result, there is an urgent need for novel, preferably optical, measurement approaches to meet the anticipated demand for a comprehensive description of inlet flow distortion for future fuselage-integrated engine concepts. Since ground tests have so far not been able to capture the entire spectrum of possible flow phenomena [13], these new techniques should also have the potential to be used for flight testing.

*Senior Scientist, Paul Scherrer Institute, ulrich.doll@psi.ch.

†Senior Scientist, Paul Scherrer Institute, ralf.kapulla@psi.ch.

‡Researcher, ILA R&D GmbH, steinbock@ila-rnd.de.

§Managing Director, ILA R&D GmbH, dues@ila-rnd.de.

¶Research Fellow, Cranfield University, matteo.migliorini@cranfield.ac.uk.

||Senior Lecturer, Cranfield University, p.zachos@cranfield.ac.uk.

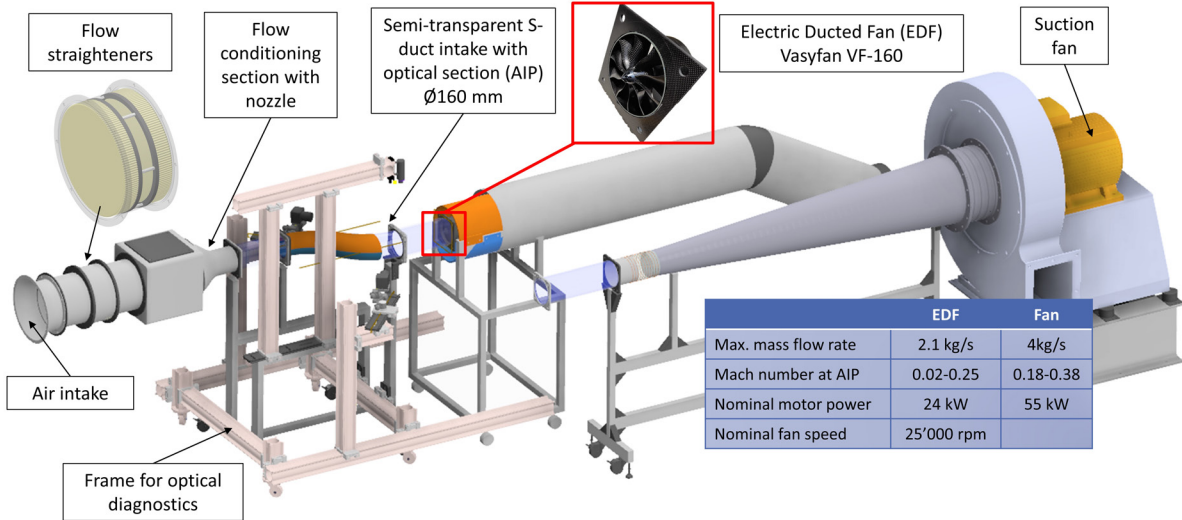


Fig. 1 3D rendering of subsonic convoluted diffuser intake test rig (CCITF).

In order to de-risk the prospective usage of new measurement technology in industrial testing and certification, a new ground test facility for investigating complex convoluted intake geometries with distorted inflow is currently installed at Cranfield University. A 3D rendering of the Cranfield Complex Intake Test Facility (CCITF) is shown in figure 1. The rig comprises in sequence a bell-mouth inlet, a set of flow straighteners and conditioners, a flow conditioning section with adjacent convergent nozzle, an inlet section, an intake and an optical section representing the Aerodynamic Interface Plane (AIP) with a diameter of 160 mm. The whole front section is movable and can be either connected to a diffuser that is coupled with a centrifugal fan outside the test house to provide the required suction. In this configuration, the test rig is designed for inlet Mach numbers of up to 0.7, resulting in a range of expected Mach number at the AIP between 0.18–0.38. Or, the movable front section can be connected to an electric ducted fan (EDF) to simulate the upstream effect of the spinning rotor on the AIP flow field. For inlet Mach numbers between 0.1–0.38, Mach numbers of up to 0.25 at the AIP can be reached in this mode of operation. The front part features a modular design so that it can accommodate a wide variety of intake geometries (e.g. straight, S-shape, serpentine). In the flow conditioning section, different gauze screens and vortex generators can be used to impose pre-defined total pressure and swirl distortion profiles on the inlet flow prior to the intake, reproducing the expected initial distortion level of BLI configurations or cross-wind conditions [14, 15]. The test section has excellent optical accessibility to allow for a flexible integration of different optical measurement techniques. All optics and measuring equipment can be mounted on a dedicated frame which is decoupled from the test section and can be easily moved with the entire instrumentation.

In a recent review article [16], an overview on the state-of-the-art in non-intrusive inlet flow diagnostics by means of laser-optical particle image velocimetry (PIV) and Doppler global velocimetry (DGV) was provided. When compared to the current industry standard [12], optical measurement methods offer much richer datasets in space and potentially in time by orders of magnitude [17–19]. However, the need for seeding as well as elevated optical access requirements for PIV limit these techniques to ground testing. One of the few laser-optical methods that do not require the addition of a flow tracer, the filtered Rayleigh scattering (FRS) technique [20] is identified as a promising candidate, since it has the proven ability to simultaneously measure time-averaged pressure, temperature and velocity fields in application-oriented test facilities with limited optical accessibility [21–24]. The combined measurement of three-component (3C) velocity fields with planar pressure and temperature was achieved by observing the measurement plane from three different sides using multiple-branch imaging fibre technology [25]. This demonstrates the inherent capabilities of the FRS technique to capture all relevant flow quantities for a comprehensive characterisation of inlet flow distortions.

Previous multi-parameter measurements by FRS relied on a frequency scanning approach [21, 26, 27], which is a time consuming data acquisition mode and can only provide time-averaged measurements results. To extend the FRS technique to the planar measurement of multiple time-resolved flow quantities, one idea is to split the scattering signal obtained from a single laser pulse between several detection channels, each equipped with a molecular filter of different vapour density [28–32]. A second approach involves using a single molecular filter in combination with at least five directions of observation to derive the five unknown flow variables from a single-pulse measurement (pressure,

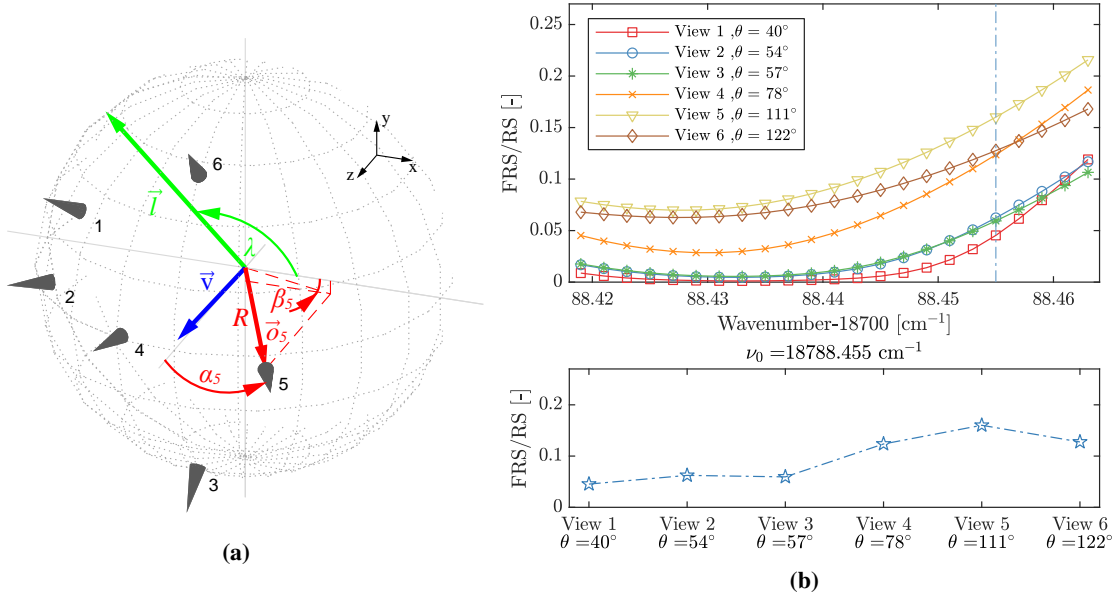


Fig. 2 (a) Orientation of the six optimised camera views on a sphere around the region of interest. (b) *Top* Simulated FRS intensity spectra normalised by the available Rayleigh scattering (RS) for a frequency scan around the 18788.44 cm^{-1} -doublet for the six optimised camera views. *Bottom* FRS signal intensities at the selected single-pulse wavenumber. The scattering angle θ is indicated in the x-axis.

temperature and three velocity components) [16]. The latter approach leads to a complex detection scheme that has recently been optimised to maximise sensitivities of an instantaneous multi-parameter FRS measurement with regard to the planned application at the CCITF based on a six-branch image fibre bundle [33]. It is the aim of this work to experimentally verify this diagnostic approach by performing FRS measurements with an optimised multiple-view detection scheme on a simplified flow configuration.

The principle idea behind the time-resolved multi-parameter FRS measurement combining various perspective views is briefly explained in section II. The actual flow experiment is a mock-up of the CCITF and is introduced in section III. In addition, the FRS instrumentation with optimised detection arrangement is presented. The post processing of the multi-view FRS data in time-averaged and time-resolved evaluation mode is outlined and results are presented and discussed in section IV. Finally, the presented work is put into context with the planned application at the CCITF.

II. Multiple-view FRS diagnostics

The general idea behind the simultaneous measurement of multiple instantaneous flow parameters from varying perspective views builds on a further development of the FRS velocimetry approach outlined in [25]. There, three linearly independent directions of observation were combined with frequency scanning to measure time-averaged 3C velocity, pressure and temperature fields in a jet flow. By scanning the laser's output frequency along the molecular filter's transmission curve, this approach resulted in a significantly over-determined mathematical problem, from which the five flow variables were obtained with high accuracy using non-linear regression. In contrast, a multi-view FRS measurement based on a single laser pulse with a single output frequency must rely on a significantly lower amount of data, corresponding to the number of available camera perspectives.

In our recently published work [33], it is argued that in a single-frequency multi-view FRS arrangement, it is not sufficient to place the different camera perspectives randomly in the space around the flow experiment. Instead, multi-objective optimisation is used to identify a suitable optical configuration to reach the lowest measurement uncertainties. A schematic containing the six optimised camera positions for a representative flow condition at the AIP in the CCITF ($p = 77.2 \text{ kPa}$, $T = 288 \text{ K}$, $\vec{v} = [-0.5, 1.5, 56] \text{ m/s}$), represented by the gray cones, in relation to the direction of the laser light \vec{l} and the flow velocity \vec{v} (observation from downstream) is depicted in figure 2a. All views are oriented on a spherical surface with radius R and their positions are defined by the respective polar and azimuthal angles α and β . The laser is aligned at an angle $\lambda = 135^\circ$ to ensure uniformly distributed uncertainties for the in-plane

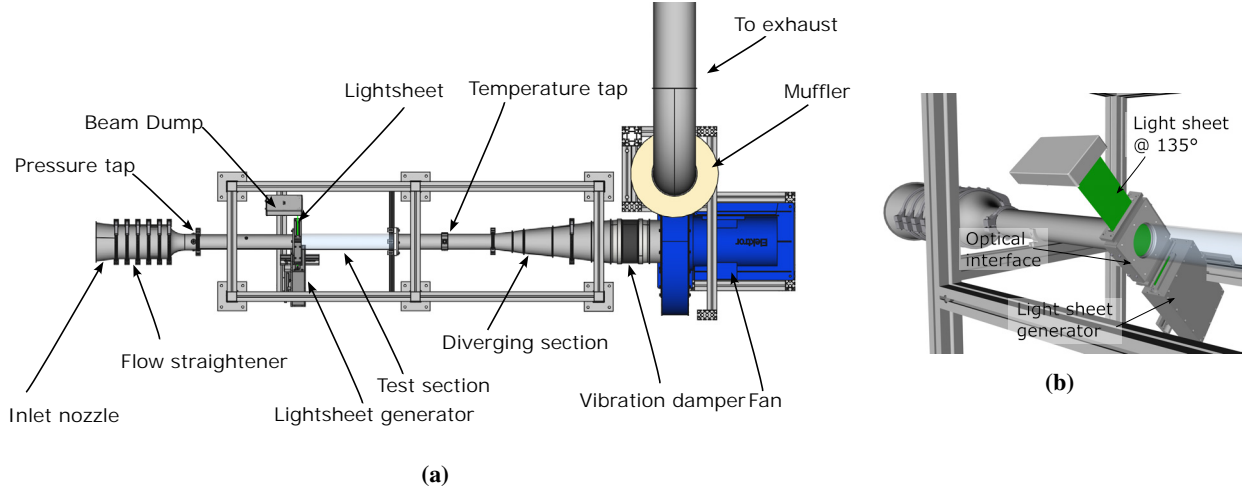


Fig. 3 (a) Schematic of the simplified flow configuration. (b) Enlarged view of the test section with light sheet interface.

velocity components. The effect the resulting scattering geometry has on the FRS signal is shown in figure 2b, *top*. A simulation is conducted for the AIP flow with different excitation wavenumbers within the blocking range of the molecular filter. All curves have in common that the FRS signal rises with wavenumber, which is related to the double structure of the selected absorption line and leads to a reduced transmitted Rayleigh intensity at lower values. The differences between the curves are predominantly related to the variation of the scattering angle θ , i.e. the angle spanned by the laser direction \vec{l} and the direction of observation \vec{o} . The scattering angle has a pronounced influence on the Rayleigh scattering's spectral width and shape, whereby the width increases or decreases with θ and the portions of the Rayleigh scattering that pass through the molecular filter become correspondingly larger or smaller.

For an instantaneous FRS measurement, one of the wavenumbers has to be selected, which is highlighted by the blue dashed-dotted line in figure 2b, *top*. The corresponding normalised FRS signal intensities are depicted in figure 2b, *bottom*. The choice is motivated by the location of the wavenumber close to the end of the blocking region of the molecular filter, where the slope of the transmission curve increases rapidly and changes in the Rayleigh scattering's spectral shape due to temperature or pressure or Doppler shifts from flow velocity lead to strong dynamics of the FRS intensity. For detailed information about the multi-variate dependency of the FRS signal on the wavenumber, the scattering angle as well as the optimised detection configuration that follows can be found in our previous work [33].

III. Simplified flow configuration and FRS instrumentation

The simplified flow configuration is intended to facilitate an initial proof of concept for the FRS system with similar optical access constraints prior to its demonstration at the CCITF, which is designed to produce substantially more complex flow topologies and higher flow rates. The test rig is designed for a bulk streamwise velocity of up to 100 m/s at the test section, which is about a quarter of the capability of the CCITF in terms of volumetric flow rate. A schematic of the flow facility is shown in figure 3a. Air is sucked into a bell-shaped inlet nozzle manufactured using fused deposition modelling 3D printing. For initial flow conditioning, a honeycomb flow straightener and three meshes are installed in front of the inlet nozzle to reduce the velocity fluctuations to about 1 % of the mean flow velocity. The incurred pressure drop over the inlet nozzle is closely connected to the flow rate and Laser Doppler anemometry (LDA) measurements are applied to yield an empirical calibration of the resulting velocities against dp . Following the inlet section, a short straight pipe homogenises the velocity and turbulence levels in the flow domain. A close-up view of the following test section is shown in figure 3b. It consists of a light-sheet interface and a precision borosilicate glass pipe of 500 mm length and 80 mm internal diameter. To introduce the laser into the test section, the light-sheet interface aims at minimising laser scattering and reflections off glass surfaces: a tiny gap is left between the inlet pipe and the glass channel, which is surrounded by a sealed housing with plane windows on the input and output flanges. The laser enters through the gap and illuminates the cross-section of the flow channel, which can then be observed from different perspectives from the downstream side.

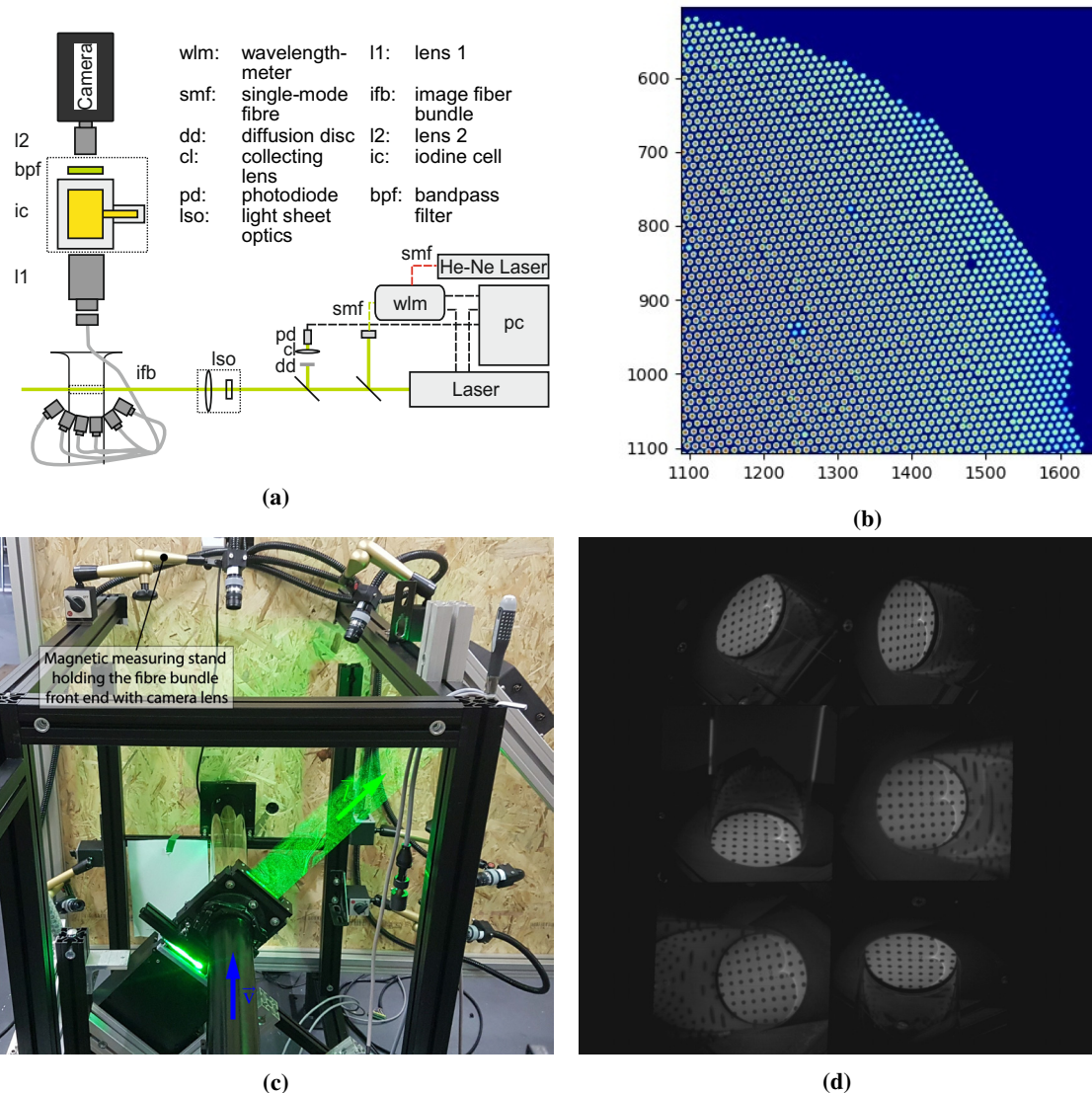


Fig. 4 (a) Principle layout of the FRS system. (b) Close-up image of a fibre bundle exit illuminated with an integrating sphere. (c) Photograph of the FRS instrumentation installed at the simplified flow facility. (d) Snapshot of a calibration target observed through the six-branch image fibre-bundle.

As outlined in the introduction, the overarching goal is the implementation of an FRS instrument for the simultaneous measurement of multiple time-resolved flow quantities. Since the current work focuses on the optimised detection setup of figure 2a, a continuous wave (CW) instead of a pulsed laser is applied here to reduce system complexity. The general layout of the FRS implementation is shown schematically in figure 4a. The system is based on a narrow-linewidth AzurLight (CW) fibre laser, emitting green laser light at a wavelength of 532 nm. The laser has an adjustable output power ranging from 0.1 to 6 W and a spectral bandwidth below 200 kHz, which is accomplished through an external NKT Photonics ADJUSTIK Y10 seed laser unit. The latter features two options for tuning the laser's output frequency: fast piezo tuning in the range of 10 GHz around the central wavelength and slow thermal tuning over 700 GHz (compared to 60 GHz of the previously used Coherent Verdi system [21]). A small portion of laser light is coupled into the wavelength monitoring and control unit through a single-mode fibre (smf) behind the laser exit. This light is used as an input signal for the frequency stabilisation of the laser, which is based on a HighFinesse WS-8 wavelength-meter (wlm), achieving a relative stability of the laser's output frequency below 1 MHz to the set-point. Since changing environmental conditions may lead to a drift of the frequency measurement, the device is repeatedly calibrated using a

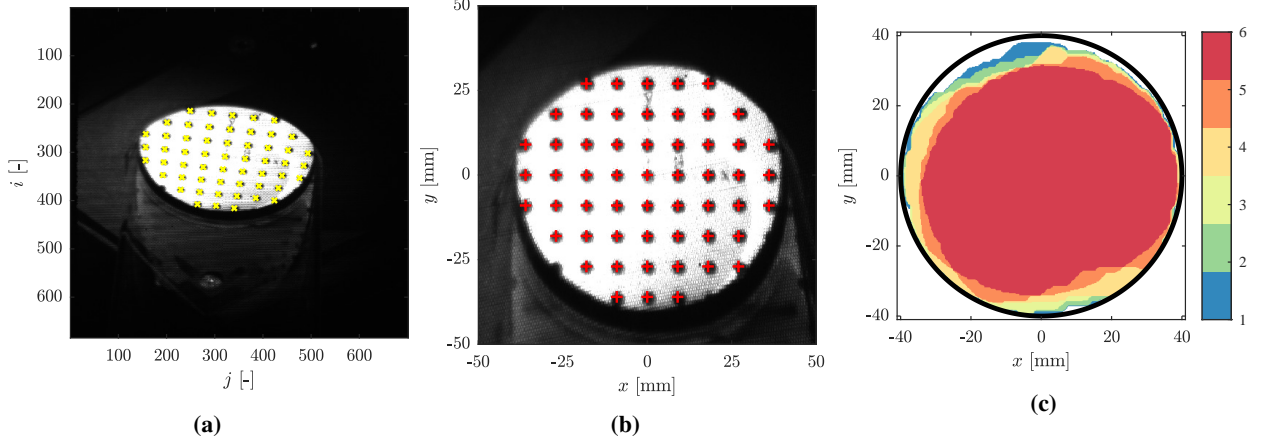


Fig. 5 Image transformation of perspective #6 from camera coordinate system (a, yellow cross) to world coordinate system (b, red plus). (c) Parts of the duct (black, solid) are obstructed from view. The number of views having optical access to a particular area is presented in false color.

narrow-linewidth, frequency stabilised helium-neon laser. As the Rayleigh scattering signal depends on the incident laser intensity, the latter is continuously monitored by a combination of a diffusion disk (dd), collecting lens (cl) and photo diode (pd). Subsequently, the laser beam is expanded into a light-sheet and illuminates the measurement plane.

Light scattered from the plane of interest is collected with a six-branch image fibre bundle (ifb). The front end of each branch is equipped with a camera lens having a focal length of 16 mm and $f_{\#} = 1.4$, imaging the observed region on a light sensitive area of $4 \times 4 \text{ mm}^2$ (400×400 fibre elements @ $10 \mu\text{m}$ fibre diameter). A close-up image of the output of an image fibre bundle branch observing the illuminated output side of an integrating sphere can be seen in figure 4b. The image shows the typical structure of a leached fibre bundle with individual fibres containing the signal intensities surrounded by dark light insensitive cladding. Each branch has a length 2500 mm so that the different perspectives can be conveniently aligned in the space around the test section. A photograph of the FRS instrumentation installed at the simplified flow facility is shown in figure 4c. When reproducing the optimised optical setup shown in figure 2a, hydraulic magnetic measuring stands are used to fix the different perspectives in their respective positions. To align the six fibre bundle front ends to the optimised coordinates, the positions are projected onto the wooden screen in the background and strings are drawn from these points towards the centre of the measurement plane. Then, the respective branch is fixed at the specified radius R from this reference point. With this procedure, any error in angular alignment is assumed to be within $\pm 5^\circ$, which was shown to have an acceptable effect on measurement accuracy [33].

The individual observation branches are combined at the back-end of the image fibre bundle, resulting in a rectangular shaped area of 12 mm height and 8 mm width (3×2 square regions, each representing a single camera view). As shown in figure 4a, two lenses in retro-arrangement (I1, I2) form the transfer optics and pass the light collected by the fibre bundle branches through a molecular iodine filter (ic) and a bandpass filter (bpf), the latter blocking both broadband background light and iodine fluorescence. With the second camera lens (I2), the filtered light is focused on the camera sensor. A sample camera image with a calibration target placed inside the flow duct is shown in figure 4d.

IV. Data processing and results

In this section, the procedure of post-processing and evaluating the data obtained by the multiple-view imaging FRS instrument is outlined. Since a CW laser is used in this work, frequency scanning is applied for data acquisition and in the first step, the complete dataset is analysed to obtain high quality time-averaged multi-parameter measurement results. In a second step, an individual wavenumbers is selected and the data is analysed in a quasi-time-resolved mode for testing the optimised six-view observation concept for single-pulse data evaluation.

A. Image processing, data analysis and time-averaged results

A dataset obtained by the multiple-view imaging FRS instrument consists of (1) a set of calibration images to determine the camera positions and to map the different perspectives onto a common Cartesian grid; (2) reference

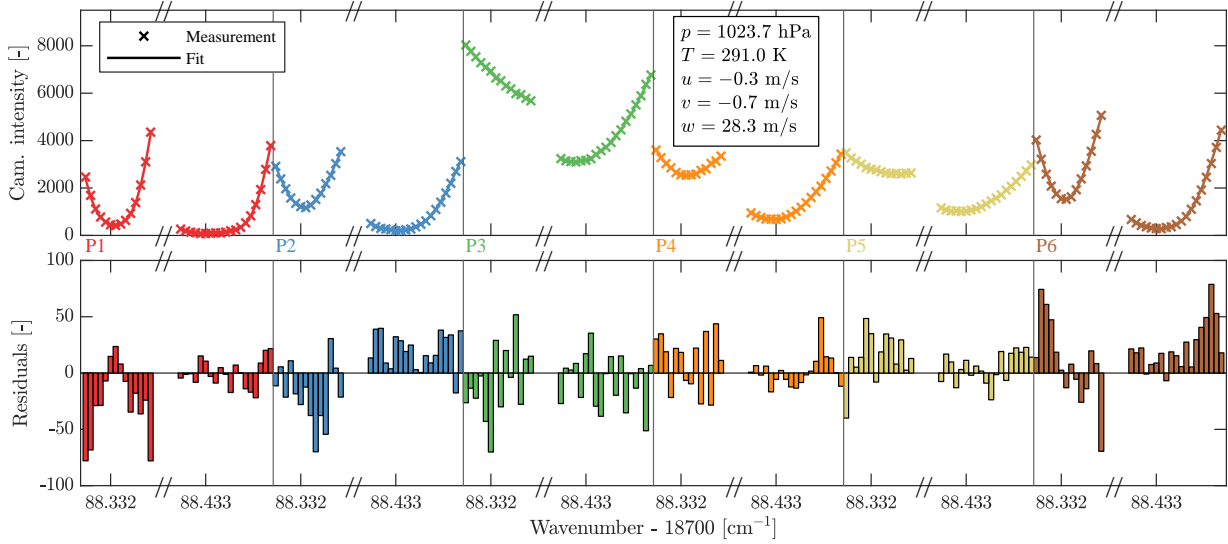


Fig. 6 *Top* Evaluation of FRS intensity spectra obtained from frequency scanning for a single super-resolution element. Each color represents a different perspective. The measured FRS intensities (crosses) are fitted with the model equation (solid) to derive pressure, temperature and u, v, w velocity components (fit result in the box). *Bottom* Residuals of the data fit.

image data acquired with pressure and temperature known (ambient conditions) and zero flow velocity to obtain an optical calibration constant, a background parameter and a zero Doppler shift to account for the absolute accuracy of the wavelength-meter (10 MHz) and frequency-dependent transmission properties of the bandpass filter at each resolution element; (3) Data obtained under flow conditions. For both reference and flow datasets, frequency scanning at 37 discrete frequencies was performed and measurements were repeated five times and averaged to further increase signal-to-noise-ratio (SNR). To evaluate the FRS data, the transmission curve of the absorption filter is required, which has been calibrated with a photodiode arrangement with an accuracy of $< 0.5\%$.

The automated identification of the six camera positions relies on Python’s OpenCV toolbox [34] and will not be discussed here. The post-processing starts with subdividing the calibration image of figure 4d into six parts, each representing a single perspective. For all these views, a dewarping procedure is applied to transform the different perspectives to a predefined coordinate system represented by a calibration plate with a regular dot-pattern introduced at the light sheet plane. The procedure is exemplary shown for the calibration image of perspective # 6 in figures 5a (warped) and 5b (dewarped). As a result, each resolution element in world coordinates covers an area of $1 \times 1 \text{ mm}^2$ and contains the information of the six perspectives. As outlined in section III, a specific flange is used to illuminate the cross section with the laser. Depending on the viewing angle, the optical access to the measuring plane is partially blocked by the housing of the light sheet flange, which is visualised in figure 5c. The red zone represents the visible area common to all views, covering over 75 % of the total cross section.

Following the camera calibration and dewarping procedures, the optical calibration constant, background parameter and zero Doppler shift per resolution element are determined separately for each camera perspective from the reference frequency scan relying on established methodology [21, 35]. For analysing the data obtained under flow conditions, the measurements from all perspectives are combined and jointly evaluated. In order to simultaneously derive pressure, temperature and the three velocity components from the measured FRS intensity spectra, a nonlinear fit of an appropriate measurement model is carried out so that the flow quantities are obtained at each super-resolution element (37 scanning frequencies \times 6 perspectives). The result of the fitting procedure for a single super-resolution element is shown in figure 6, *top*. Measurement data are obtained at two neighboring absorption lines, leading to a two-branch structure with a frequency gap in between. The resulting intensity spectra for each perspective strongly differ in level and shape, which is mainly related to the variation in scattering geometry and its influence on the Rayleigh lineshape [33]. The Rayleigh lineshape model used in this work is a combination of a calibrated analytical model [35] and a recently introduced machine learning approximation [36]. In contrast to the previous approach, where the Doppler frequencies were fitted and the 3C velocity field was subsequently reconstructed [25], here, the Doppler formula is coupled with the simulation

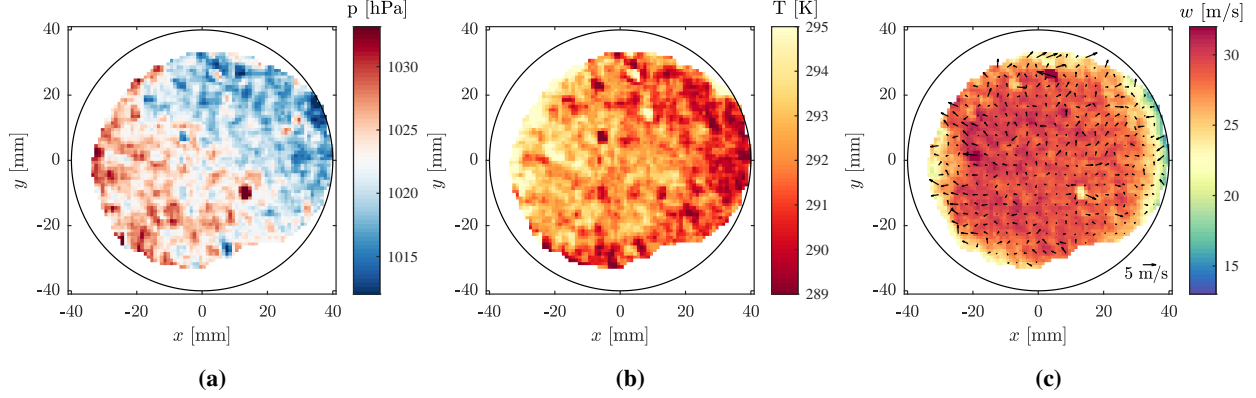


Fig. 7 Time-averaged pressure (a), temperature (b) and axial velocity maps (c) for $dp = 5.9$ hPa. Vectors in (c) represent the in-plane velocity components, only every 3rd vector is shown. The channel boundaries are indicated by the black solid line.

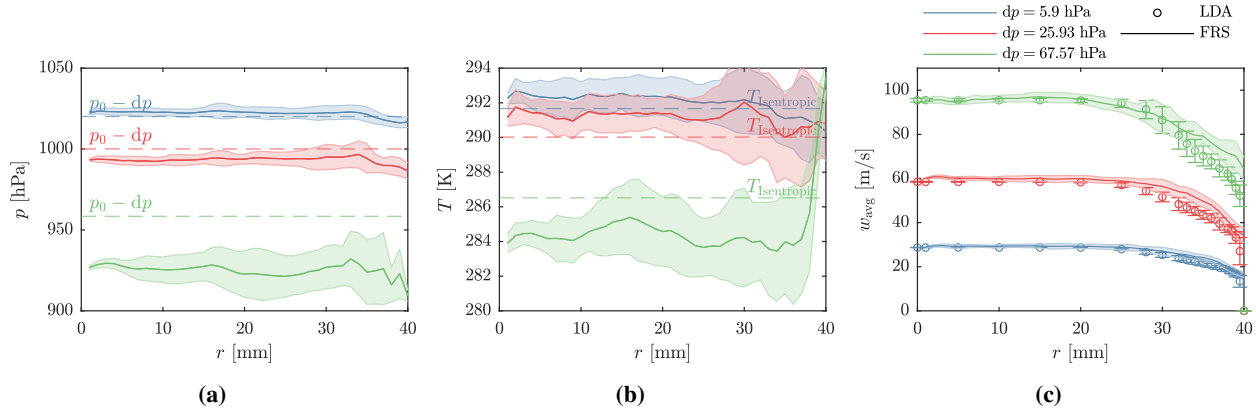


Fig. 8 Radially averaged pressure profiles (solid) with $p_0 - dp$ (dashed) (a), temperature profiles (solid) with isentropic temperature (dashed) (b) and axial velocity profiles (solid) with LDA measurements (circle) (c) for three operating points denoted by the differential pressure dp . The shaded areas and LDA errorbars in (c) indicate the standard deviation of the radial mean per radius.

of the FRS intensities. This has the distinct advantage that the maximum number of unknown flow parameters is fixed to five, regardless of the number of perspectives, whereas when fitting Doppler shifts, the number of unknowns increases with the number of perspectives. A Levenberg-Marquardt algorithm is used to fit the modelled FRS intensity spectra to the measured data in a least-squares sense, yielding temperature, pressure and the three velocity components for each super-resolution element. The residuals of the fitting procedure shown in figure 6, *bottom*, demonstrate the very good quality of the fit and are of the order of 0.7% of the FRS intensity averaged over all frequencies.

Pressure, temperature and axial velocity maps determined from the outlined methodology are shown in figure 7. The results show the typical structure of a evolving pipe flow, with almost constant static pressure and temperature over the entire cross section and a “plug-like” axial velocity distribution, with constant values in the center and a steep gradient towards the channel walls. The pressure and temperature fields exhibit a weak non-physical structure, possibly caused by uncertainties in the automated camera localisation or an insufficient background correction; however, these deviations lie on average below 0.5% of the corresponding mean pressure and temperature over the cross-section. In addition to the axial velocity component w , the velocity map in figure 7c also contains the in-plane components u and v indicated by the vectors. As expected for the examined flow, there exists no lateral flow velocity and the randomly oriented velocity vectors are related to the uncertainty of the method.

To further assess the quality of the FRS measurements, radially averaged pressure, temperature and axial velocity profiles are compared to the reference differential pressure dp measured at the inlet nozzle, the resulting isentropic

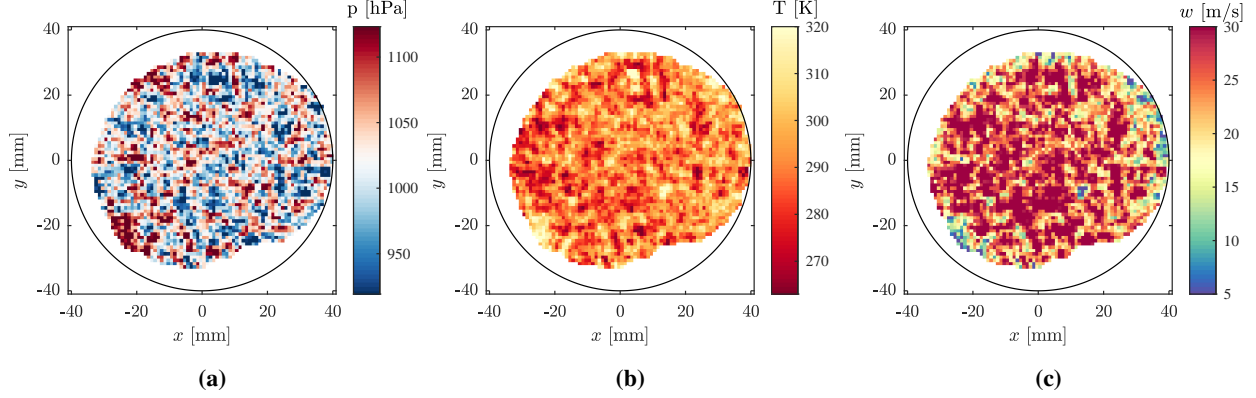


Fig. 9 Quasi time-resolved pressure (a), temperature (b) and axial velocity maps (c) for $dp = 5.9$ hPa. The channel boundaries are indicated by the black solid line.

temperature and corresponding laser Doppler anemometry (LDA) velocity measurements for three operating points in figure 8. For $dp = 5.9$ and $dp = 25.93$ hPa, deviations of pressure and temperature fall within 1% and below 0.5% of their corresponding reference value. For $dp = 67.57$ hPa, differences grow to about 3% in pressure and 0.7% in temperature and an artifact appears in the temperature profile between $r = 37$ and 40 mm. The reason for the deterioration of the quality in the case of operating point $dp = 67.57$ hPa is probably related to the large time interval to the reference measurement of about 24 hours, whereas the other two conditions were measured immediately afterwards. Regarding the comparison of axial velocities measured by LDA and FRS, there is an excellent agreement between both methods for all operating points up to a radial distance of $r = 25$ mm. The deviations when approaching the boundaries can be explained by the differing measurement location, which in case of LDA was 2-3 tube diameters downstream, resulting in a more developed velocity profile with a smaller area of constant velocity near the center and less steep slopes towards the channel border.

Spatially averaged and statistical quantities obtained from the area of constant flow parameters around the tube axis for operating point $dp = 5.9$ hPa are combined in table 1. As stated before, reference values and the spatial averages determined for the frequency scanning FRS results are in excellent agreement. Standard deviations are 2.3 hPa, 0.96 K and 0.7 m/s for pressure, temperature and axial velocity, respectively, and agree well with the results from a Monte-Carlo analysis used to estimate the expected level of measurement uncertainty.

B. Quasi time-resolved data analysis

To verify the validity of the presented multi-view imaging concept for the combined determination of multiple time-resolved flow quantities, the data analysis is now performed for a single excitation frequency used in the optimisation of the six camera perspectives. In consequence, the number of available FRS intensities per super-resolution element reduces from 222 (6 perspectives times 37 frequencies) to 6 (6 perspectives times 1 frequency). The quasi time-resolved single-frequency analysis utilises the optical calibration constant, the background parameter and the zero Doppler shift determined during the evaluation of the time-averaged data.

Resulting pressure, temperature and axial velocity fields for the quasi time-resolved analysis at operating point $dp = 5.9$ hPa are shown in figure 9. Again, the expected distribution of constant pressure and temperature can be observed. However, in comparison to the frequency scanning results of figure 7, where spatial variations are less than 1% over the cross section, the variations in the quasi time-resolved results rise to about 10%. A similar behaviour can be observed for the axial velocity, which appears less smooth than the corresponding frequency scanning results.

Despite the overall lower quality of the quasi time-resolved measurement results, the spatial averages in table 1 are in very good agreement with the reference data. The standard deviations confirm the previously stated trend and are significantly higher than the corresponding results of the frequency scanning. Considerable deviations from the spatial standard deviations can be observed in the theoretical uncertainties calculated with Monte Carlo, which could indicate an error in the noise simulation and will be the subject of further investigations.

Table 1 Comparison of reference pressure ($p_0 - dp$), temperature ($T_{\text{isentropic}}$) and axial velocity (LDA) with FRS spatial averages (avg) and standard deviations (σ_s) an area of constant flow parameters) for operating point $dp = 5.9$ hPa. Standard deviations σ_{MC} are theoretical values computed from Monte Carlo simulations based on the FRS data’s SNR.

	p [hPa]			T [K]			w [m/s]		
	avg	σ_s	σ_{MC}	avg	σ_s	σ_{MC}	avg	σ_s	σ_{MC}
Reference	1020	-	-	291.7	-	-	28.7	-	-
Frequency scan	1023	2.3	1.2	292	0.96	0.7	29	0.7	1.1
Quasi time-resolved	1021	52	100	291	9.5	16	27	5.2	10

V. Conclusions

Propulsion system integration will play a central role in developing feasible future aircraft architectures to ensure safe, reliable and efficient operation. An important enabler to the successful development and integration of these novel systems is leveraging the unique capabilities of imaging based laser-optical flow diagnostics. In this context, the filtered Rayleigh scattering (FRS) technique has been identified as a promising candidate since the method does not require the addition of flow tracers and has the capability for the combined planar measurement of three-component velocity and scalar fields.

In our previous work published earlier this year, we developed an FRS concept for the simultaneous time-resolved measurement of 3C velocity, pressure and temperature fields by detecting the FRS signal from six perspective views. The perspectives were optimised to yield the lowest measurement uncertainties in a time-resolved single-frequency measurement scenario. To verify this concept, an FRS instrument is installed at a simplified duct flow facility, making use of multiple-branch image fibre bundle technology to realise signal detection from six perspectives. To reduce system complexity, FRS measurements are carried out using a continuous wave laser and frequency scanning is applied to obtain time-averaged measurement results. The latter express low uncertainties of 2.3 hPa, 1 K and 0.7 m/s in static pressure, temperature and axial flow velocity, respectively, and are in excellent agreement with LDA velocity and pressure probe measurements as well as analytical temperature calculations. To demonstrate the detection concept for time-resolved measurements, quasi time resolution is simulated by selecting a single frequency from the frequency scan and performing a multi-parameter analysis on this reduced dataset. The 3C velocity, pressure and temperature results thus obtained are in good agreement with the benchmark values on average, but exhibit much greater uncertainties compared to the frequency scanning results.

The outcome of this study is an important milestone to qualify the FRS method for characterising complex inlet flow distortion patterns in the CCITF. Moreover, the presented results provide invaluable insights into the capabilities of FRS for multi-parameter measurements based on a single excitation frequency and future work will focus on applying pulsed laser radiation for the true combined time-resolved measurement of 3C velocity, pressure and temperature fields by FRS.

Acknowledgments

The SINATRA project leading to this publication has received funding from the Clean Sky 2 Joint Undertaking (JU) under grant agreement No 886521. The JU receives support from the European Union’s Horizon 2020 research and innovation programme and the Clean Sky 2 JU members other than the Union.

References

- [1] European Commission – Directorate General for Research and Innovation & Directorate General for Mobility and Transport., *Flightpath 2050: Europe’s vision for aviation*, The Publications Office of the European Union, Luxembourg, 2011. <https://doi.org/10.2777/50266>.
- [2] “NASA Strategic Implementation Plan - 2019 Update,” Tech. rep., 2019. URL <https://www.nasa.gov/sites/default/files/atoms/files/sip-2019-v7-web.pdf>.
- [3] “Strategic Research and Innovation Agenda - 2017 Update,” Tech. rep., 2017. URL <https://www.acare4europe.org/sites/acare4europe.org/files/document/ACARE-Strategic-Research-Innovation-Volume-1.pdf>.

- [4] Kim, H. D., Felder, J. L., and Armstrong, M., “Revolutionary Aeropropulsion Concept for Sustainable Aviation: Turboelectric Distributed Propulsion,” *XXI International Symposium on Air Breathing Engines (ISABE)*, Busan, Korea, 2013. URL <https://core.ac.uk/display/42733509>.
- [5] Uranga, A., Drela, M., Greitzer, E. M., Hall, D. K., Titchener, N. A., Lieu, M. K., Siu, N. M., Casses, C., Huang, A. C., Gatlin, G. M., and Hannon, J. A., “Boundary Layer Ingestion Benefit of the D8 Transport Aircraft,” *AIAA Journal*, Vol. 55, No. 11, 2017, pp. 3693–3708. <https://doi.org/10.2514/1.J055755>.
- [6] Seitz, A., Habermann, A. L., Peter, F., Troeltsch, F., Castillo Pardo, A., Della Corte, B., van Sluis, M., Goraj, Z., Kowalski, M., Zhao, X., Grönstedt, T., Bijewitz, J., and Wortmann, G., “Proof of Concept Study for Fuselage Boundary Layer Ingesting Propulsion,” *Aerospace*, Vol. 8, No. 1, 2021. <https://doi.org/10.3390/aerospace8010016>.
- [7] Wellborn, S. R., Reichert, B. A., and Okiishi, T. H., “Study of the compressible flow in a diffusing S-duct,” *Journal of Propulsion and Power*, Vol. 10, No. 5, 1994, pp. 668–675. <https://doi.org/10.2514/3.23778>.
- [8] Cousins, W. T., “History, Philosophy, Physics, and Future Directions of Aircraft Propulsion System/Inlet Integration,” *ASME Turbo Expo: Turbine Technical Conference and Exposition*, Vol. 2, American Society of Mechanical Engineers, Vienna, Austria, 2004. <https://doi.org/10.1115/GT2004-54210>.
- [9] S-16 Turbine Engine Inlet Flow Distortion Committee, “Inlet Total-Pressure-Distortion Considerations for Gas-Turbine Engines, AIR1419C,” Tech. rep., 2017. <https://doi.org/10.4271/AIR1419C>.
- [10] S-16 Turbine Engine Inlet Flow Distortion Committee, “A Methodology for Assessing Inlet Swirl Distortion, AIR5686,” Tech. rep., 2017. <https://doi.org/10.4271/AIR5686>.
- [11] Migliorini, M., Zachos, P. K., and MacManus, D. G., “Novel Method for Evaluating Intake Unsteady Flow Distortion,” *Journal of Propulsion and Power*, Vol. 38, No. 1, 2021, pp. 135–147. <https://doi.org/10.2514/1.B38127>.
- [12] S-16 Turbine Engine Inlet Flow Distortion Committee, “Gas Turbine Engine Inlet Flow Distortion Guidelines, ARP1420C,” Tech. rep., 2017. <https://doi.org/10.4271/ARP1420C>.
- [13] S-16 Turbine Engine Inlet Flow Distortion Committee, “Inlet/Engine Compatibility - From Model to Full Scale Development, AIR5687A,” Tech. rep., 2016. <https://doi.org/10.4271/air5687a>.
- [14] McLelland, G., MacManus, D. G., Zachos, P. K., Gil-Prieto, D., and Migliorini, M., “Influence of Upstream Total Pressure Profiles on S-Duct Intake Flow Distortion,” *Journal of Propulsion and Power*, Vol. 36, No. 3, 2020, pp. 346–356. <https://doi.org/10.2514/1.B37554>.
- [15] Migliorini, M., Zachos, P. K., MacManus, D. G., and Haladuda, P., “S-duct flow distortion with non-uniform inlet conditions,” *Proceedings of the Institution of Mechanical Engineers, Part G: Journal of Aerospace Engineering*, 2022, p. 09544100221101669. <https://doi.org/10.1177/09544100221101669>, publisher: IMECHE.
- [16] Doll, U., Migliorini, M., Baikie, J., Zachos, P. K., Röhle, I., Melnikov, S., Steinbock, J., Dues, M., Kapulla, R., MacManus, D. G., and Lawson, N. J., “Non-intrusive flow diagnostics for unsteady inlet flow distortion measurements in novel aircraft architectures,” *Progress in Aerospace Sciences*, Vol. 130, 2022, p. 100810. <https://doi.org/10.1016/j.paerosci.2022.100810>.
- [17] Zachos, P. K., MacManus, D. G., Prieto, D. G., and Chiereghin, N., “Flow Distortion Measurements in Convoluted Aeroengine Intakes,” *AIAA Journal*, Vol. 54, No. 9, 2016, pp. 2819–2832. <https://doi.org/10.2514/1.J054904>, publisher: American Institute of Aeronautics and Astronautics.
- [18] Guimarães, T., Lowe, K. T., and O’Brien, W. F., “StreamVane Turbofan Inlet Swirl Distortion Generator: Mean Flow and Turbulence Structure,” *J. Propuls. Power*, Vol. 34, No. 2, 2018, pp. 340–353. <https://doi.org/10.2514/1.B36422>, publisher: American Institute of Aeronautics and Astronautics.
- [19] Gil-Prieto, D., MacManus, D. G., Zachos, P. K., and Bautista, A., “Assessment methods for unsteady flow distortion in aero-engine intakes,” *Aerosp. Sci. Technol.*, Vol. 72, 2018, pp. 292–304. <https://doi.org/10.1016/j.ast.2017.10.029>.
- [20] Miles, R., and Lempert, W., “Two-dimensional measurement of density, velocity, and temperature in turbulent high-speed air flows by UV Rayleigh scattering,” *Applied Physics B Photophysics and Laser Chemistry*, Vol. 51, No. 1, 1990, pp. 1–7. <https://doi.org/10.1007/BF00332317>.
- [21] Doll, U., Stockhausen, G., and Willert, C., “Endoscopic filtered Rayleigh scattering for the analysis of ducted gas flows,” *Experiments in Fluids*, Vol. 55, No. 3, 2014. <https://doi.org/10.1007/s00348-014-1690-z>.

- [22] Doll, U., Stockhausen, G., Heinze, J., Meier, U., Hassa, C., and Bagchi, I., “Temperature measurements at the outlet of a lean burn single-sector combustor by laser optical methods,” *Journal of Engineering for Gas Turbines and Power*, Vol. 139, No. 2, 2017. <https://doi.org/10.1115/1.4034355>.
- [23] Schroll, M., Doll, U., Stockhausen, G., Meier, U., Willert, C., Hassa, C., and Bagchi, I., “Flow field characterization at the outlet of a lean burn single-sector combustor by laser-optical methods,” *Journal of Engineering for Gas Turbines and Power*, Vol. 139, No. 1, 2017. <https://doi.org/10.1115/1.4034040>.
- [24] Doll, U., Dues, M., Bacci, T., Picchi, A., Stockhausen, G., and Willert, C., “Aero-thermal flow characterization downstream of an NGV cascade by five-hole probe and filtered Rayleigh scattering measurements,” *Experiments in Fluids*, Vol. 59, No. 10, 2018, p. 150. <https://doi.org/10.1007/s00348-018-2607-z>.
- [25] Doll, U., Stockhausen, G., and Willert, C., “Pressure, temperature, and three-component velocity fields by filtered Rayleigh scattering velocimetry,” *Optics Letters*, Vol. 42, No. 19, 2017, pp. 3773–3776. <https://doi.org/10.1364/OL.42.003773>.
- [26] Forkey, J. N., Finkelstein, N. D., Lempert, W. R., and Miles, R. B., “Demonstration and characterization of filtered Rayleigh scattering for planar velocity measurements,” *AIAA Journal*, Vol. 34, No. 3, 1996, pp. 442–448. <https://doi.org/10.2514/3.13087>.
- [27] Boguszko, M., and Elliott, G. S., “On the use of filtered Rayleigh scattering for measurements in compressible flows and thermal fields,” *Experiments in Fluids*, Vol. 38, No. 1, 2005, pp. 33–49. <https://doi.org/10.1007/s00348-004-0881-4>.
- [28] Miles, R., and Lempert, W., “Flow diagnostics in unseeded air,” *28th Aerospace Sciences Meeting*, American Institute of Aeronautics and Astronautics, Reno, USA, 1990. <https://doi.org/10.2514/6.1990-624>.
- [29] Boguszko, M. G., “Measurements In Fluid Flows Using Filtered Rayleigh Scattering,” Ph.D. thesis, Rutgers, The State University of New Jersey, 2003.
- [30] Yeaton, I., Maisto, P., and Lowe, K., “Time Resolved Filtered Rayleigh Scattering for Temperature and Density Measurements,” *28th Aerodynamic Measurement Technology, Ground Testing, and Flight Testing Conference*, American Institute of Aeronautics and Astronautics, New Orleans, USA, 2012. <https://doi.org/10.2514/6.2012-3200>.
- [31] George, J., Jenkins, T. P., and Sutton, J. A., “Simultaneous Multi-Property Laser Diagnostics using Filtered Rayleigh Scattering,” *32nd AIAA Aerodynamic Measurement Technology and Ground Testing Conference*, American Institute of Aeronautics and Astronautics, Washington, D.C., 2016. <https://doi.org/10.2514/6.2016-3110>.
- [32] Jenkins, T. P., George, J., Feng, D., and Miles, R. B., “Filtered Rayleigh Scattering for Instantaneous Measurements of Pressure and Temperature in Gaseous Flows,” *AIAA Scitech 2019 Forum*, American Institute of Aeronautics and Astronautics, San Diego, USA, 2019. <https://doi.org/10.2514/6.2019-1324>.
- [33] Doll, U., Röhle, I., Dues, M., and Kapulla, R., “Time-resolved multi-parameter flow diagnostics by filtered Rayleigh scattering: system design through multi-objective optimisation,” *Measurement Science and Technology*, Vol. 33, No. 10, 2022. <https://doi.org/10.1088/1361-6501/ac7cca>.
- [34] Bradski, G., “The OpenCV Library,” *Dr. Dobbs Journal of Software Tools*, 2000.
- [35] Doll, U., Burow, E., Stockhausen, G., and Willert, C., “Methods to improve pressure, temperature and velocity accuracies of filtered Rayleigh scattering measurements in gaseous flows,” *Measurement Science and Technology*, Vol. 27, No. 12, 2016, p. 125204. <https://doi.org/10.1088/0957-0233/27/12/125204>.
- [36] Hunt, G. J., Ground, C. R., and Hunt, R. L., “Fast approximations of spectral lineshapes to enable optimization of a filtered Rayleigh scattering experiment,” *Measurement Science and Technology*, Vol. 31, No. 9, 2020, p. 095203. <https://doi.org/10.1088/1361-6501/ab8a7e>, publisher: IOP Publishing.